Bachelor Thesis

Quantum-state detection of electrons on liquid helium by the resonant image charge method

submitted by

Jakob Kraus

at the

Mathematisch-Naturwissenschaftliche Sektion
Fachbereich Physik

Supervised by
Prof. Paul Leiderer, Universität Konstanz
Prof. Denis Konstantinov, Okinawa Institute of Science and Technology

沖縄 (Okinawa)/Konstanz, 2023

Zusammenfassung

In der folgenden Arbeit wird eine Messapparatur vorgestellt und kontruiert, die die Sensitivität der Messung von Bildladungsströmen erhöht. Die Elektronen werden bei niedrigen Temperaturen ($< 1\,\mathrm{K}$) auf einem zur Hälfte mit suprafluidem Helium gefüllten Kondensator deponiert und bilden gebundene Rydberg-Zustände aus. Die Anregung der Zustände wird durch Bestrahlung mit modulierten Mikrowellen erreicht. Eine periodische Änderung der im Helium induzierten Bildladung wird mit einem Lock-in-Verstärker bei Raumtemperatur gemessen. Um die Empfindlichkeit der Messung zu verbessern, werden ein Schwingkreis und ein kryogener Vorverstärker konstruiert und in einem Experiment in einem Plattenkondensator getestet. Der Verstärker ist mit einem helikalem Resonator verbunden, der mit der Experimentenkammer einen Schwingkreis bildet. Bei der Messung des Bildladungssignals des 2-1-Rydberg-Übergangs wurde ein Signal-Rausch-Verhältnis von 34 dB ermittelt und eine Empfindlichkeit von 18 Elektronen berechnet, wenn der gleiche Messaufbau in einem Mikrokanalgerät verwendet wird. Verbesserungen in der Sensitivität können durch Erhöhung der Güte des Resonators, die Verringerung der Streukapazität im Design und dem Abstimmen von Spannungs- und Stromrauschen im Schaltungsdesign erreicht werden.

Abstract

In the following work, progress towards the detection of the image charge current generated by a single electron in Rydberg states on liquid helium has been made. The electrons are deposited at low temperatures ($< 1\,\mathrm{K}$) on a capacitor filled half-way with superfluid helium and form bound Rydberg states. Excitation of the states is achieved by applying modulated microwaves to drive the transition. The periodic change in the image charge in the helium is detected by a lock-in amplifier at room temperature. To improve the sensitivity of the setup, a resonant circuit and a novel cryogenic pre-amplifier design is constructed and tested in an experiment in a parallel plate capacitor structure. The amplifier is connected to a helical resonator which forms a resonant (LC-) circuit with the cell. We find a signal to noise ratio of 34 dB when measuring the image charge signal of the 2-1 Rydberg transition and calculated an estimated sensitivity of 18 electrons, when employing the same measurement setup in a micro-channel device. Further improvements involve increasing the quality factor of the resonator, reducing stray capacitance in the design and balancing voltage and current noise in the circuit design.

Acknowledgment

First and foremost, I'd like to express my gratitude to my kind and generous supervisors Paul Leiderer and Denis Konstantinov, who gave me the opportunity to work in an outstanding scientific environment, as well as to experience such a culturally rich and exciting place that is Okinawa. I'm especially indebted to Misha, who worked tirelessly to guide me through the theory, experimental work and construction of various devices in order to complete this project. For the insightful discussions about physics, life and a plethora of other topics, I'd like to thank Ivan, Jui-Yin, Kirill, and Mohamed. Last but very much not least, I'm forever grateful for all the support from the people in the OIST community and the wonderful friends I made along the way.

Contents

1 Introduction

Before the invention of computers, performing mathematical calculations were time consuming and tedious. As technology progressed, more complex machines were created to do computations, first mechanical, then electronic. With the advent of modern computers, performing a mathematical calculation is cheap and fast, which enables scientists to perform numerical analysis with millions of calculations per second. But in complex applications, like fluid dynamics, molecular simulations, combinatory problems or simulation of quantum systems, classical computers struggle, since the computing time often increases exponentially. In 1984, famous physicist and public persona Richard Feynman suggested the use of computers based on principles of quantum mechanics for solving these sets of problems. A quantum bit, often abbreviated as qubit, can exist in a superposition of multiple states, which can therefore assume multiple states of the system and is only evaluated at the end of the computation.

The biggest hurdle however in achieving efficient quantum computer is technological. Trapping and confining a suitable qubit, as well as being able to prepare its initial state, read out the final state and control the interaction with other qubits is extremely difficult. Current generation supercomputers based on superconducting Josephson Junctions are still in the noisy-intermediate-scale. In 1999, Platzman et al. [1] suggested the use of electrons bound in Rydberg-like surface states on superfluid helium at low temperatures. Qubits based on the electron Rydberg or spin states would have extremely long decoherence times due to very low interaction with their environment and can be easily manipulated. The successful implementation of such a qubit has yet to be achieved. This work aims to contribute to improving the detection mechanism of the spin state of surface electrons by the image charge method [2] by constructing a tuned resonant circuit coupled to a cryogenic amplifier.

2 Electrons on Helium

This chapter gives a brief overview of the past research efforts and introduces the basic theory for surface bound electrons on helium.

2.1 A short history

When electrons are in the proximity of a dielectric substance, the electric field will induce an image charge, which in turn attract the electron. This effect between electrons and neutrally charged materials has been known to physicists for a long time, but it didn't prove interesting for research since impurities on the surface material disturb the interaction between electrons. In the late 1960s however it was discovered, that superfluid helium at low temperatures provides an exquisitely pure system to study two-dimensional strongly correlated electron systems. [3, 4]

The image charge induced into the helium from nearby electrons confines them onto the surface; they exhibit high mobility along the plane of the interface, but their vertical motion is restricted to quantized states. The existence and properties of these surface bound states were first described theoretically in 1969 by Cole et al. [5] and Shikin [6] in 1970. This lead to increased interest in the field. A visual proof of the existence of surface bound electrons was given by Williams et al. [7] when they observed a depression on the surface caused by the deposited electrons (see Fig. 2.1). Transport properties were investigated by Sommer and Tanner [8] amongst others and the quantized states by Crandall [9] and Cole [10]. It was also discovered, that the 2D high-density electron liquid can condense into a solid structure as proposed by Wigner in 1934. Evidence of this crystallization was reported by Grimes and Adams in 1979 [11]. The Wigner solid state as well has been subject to further studies since.

In 1999, Platzman et al. [1] proposed a novel method to construct qubits from floating electrons on helium, confined by electrodes underneath the surface to create a potential which corresponds to the lattice constant of the Wigner solid state as to trap only one electron per electrode. This work has sparked an ever increasing interest in realizing qubits using surface electrons and layed the foundation for the purpose of this thesis.

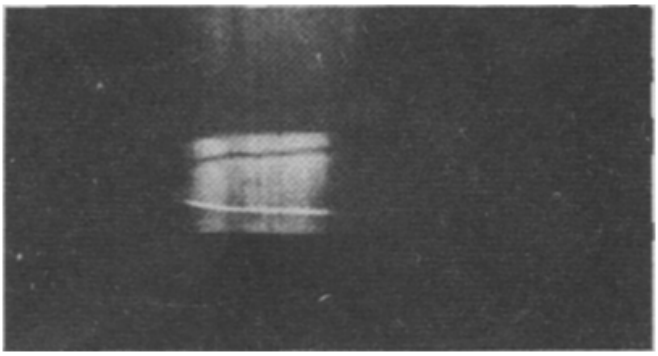

Figure 2.1: Depression of the liquid helium surface as observed by Williams et al [7]. The picture is taken at about 10° above the horizontal plane. Underneath the helium surface, a circular electrode with a positive bias is placed. Only a part of the depression is visible.

2.2 Quantum mechanical description

As a simplified system, let us consider a single electron floating above a large liquid helium surface, so we can neglect boundary effects. The electric field of the electron will polarize the helium atoms and thus induce a positive image charge, which in turn exerts an attractive force on the electron. At short distance to the interface however, the electrons occupying the 1s orbitals of the helium atoms prevent surface electrons from entering the liquid due to the Pauli exclusion principle. These opposing forces create a potential well, in which bound states can form.

If we assume a flat surface, we can separate the vertical motion from the in-plane motion completely. For the vertical position z of the electrons above the surface ($z = 0$), we can model a potential $V(z)$

$$V(z) = V_0\theta(-z) - \frac{\Lambda}{z + z_0}\theta(z) \tag{2.1}$$

where $\theta(z)$ is the heaviside step function. The first term corresponds to the strong repulsive barrier at the interface, which has been empirically determined to approximately 1 eV. The attractive term is a coulomb force where we used

$$\Lambda = \frac{e^2(\varepsilon - 1)}{4(\varepsilon + 1)} \tag{2.2}$$

as the coefficient. It has been also established to introduce an offset z_0 to avoid a singularity at the $z = 0$ and shift the potential. The value is then determined empirically by adjusting the solution to low energy states that are close to the interface. Importantly, it was found in the order of 1 Å, which is much smaller than the mean distance $\langle z \rangle$ of electrons from the surface.

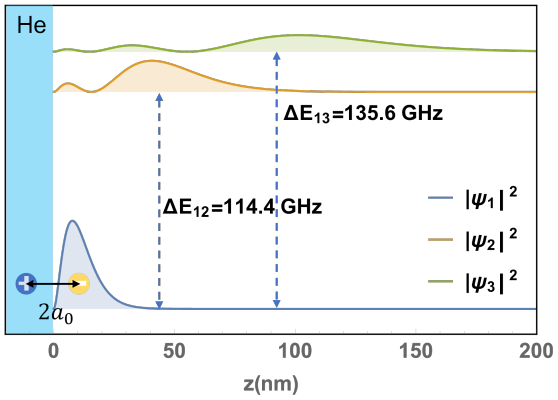

Figure 2.2: Wave functions and transition frequencies of a single electron floating atop the helium surface without additional electric field. The wave functions are identical to the radial solution of the hydrogen atom. Image reproduced from [4].

With the given potential, we can construct the Hamiltonian

$$H = -\frac{\hbar^2}{2m_e}\frac{\partial^2}{\partial z^2} + V(z) \tag{2.3}$$

for the motion in z direction. Analogous to the radial solution of the hydrogen Atom, we introduce a Bohr radius a_0 and a Rydberg constant R_y to

$$a_0 = \frac{\hbar^2}{\Lambda m_e} \tag{2.4}$$

$$R_y = \frac{m_e \Lambda^2}{2\hbar^2} \tag{2.5}$$

and can write the stationary Schrödinger equation with dimensionless coordinates z/a_0 and energy E_n/R_y. Assuming an infinite potential barrier V_0 at the interface and a negligible offset z_0 to simplify the calculation, this yields exactly the same solution as the radial part of the hydrogen atom with eigen-energies

$$E_n = -\frac{R_y}{n} = \frac{m_e \Lambda^2}{2\hbar^2 n^2} \tag{2.6}$$

for integers n denoting the level. The temperature corresponding to the thermal energy of one Rydberg constant R_y calculates to $T = E_y/k_B = 7.6\,\mathrm{K}$. Since experiments take place typically at 1 K or lower, all electrons will be in the ground state, forming a two-dimensional system.

The wavefunctions are analogous to the radial wave functions of the hydrogen atom, which consist of the Laguerre polynomials. The wave functions and transition frequencies for the first three levels n are plotted in Fig. 2.2.

This approximate solution is a good model for understanding the way free electrons form

bound states on the surface. However in experiments, we often apply an additional electric field for two reasons. Firstly, the image charge in ^{4}He $q_i = e(\varepsilon_4 - 1)/(\varepsilon_4 + 1)$ is much smaller than one electron charge $-e$, since the relative permittivity of ^{4}He is very close to unity ($\varepsilon_4 = 1.056$). This makes the attractive force quite weak, so we use an electric field to pull electrons to the surface during deposition. Secondly, applying an electric field allows us to shift the Rydberg spectrum and tune it to resonance by making use of the Stark effect. We assume a nearly homogeneous field in the area of interest and add a linear term $eE_\perp z$ which is attractive for $E_\perp > 0$. The new potential then is

$$V(z) = V_0\theta(-z) - \frac{\Lambda}{z + z_0}\theta(z) + eE_\perp z \tag{2.7}$$

Solving the equation of motion for this potential is more tricky. We can make approximations for a weak $E_\perp$ using an perturbation theory approach, and for a strong electric field, where the attraction by the image charge potential is negligible. For the perturbative ansatz, we assume a linear shift in the energy levels like

$$\delta E_n \approx eE_\perp \langle n|z|n\rangle \tag{2.8}$$

where $\langle n|z|n\rangle$ is the mean distance of the electron for a given quantum number n. This approach allows for small corrections and has been used successfully to tune the electrons into resonance when applying microwave radiation. In this model, the transition energies increase with higher field because of the dependence in the mean distance z which increases with higher levels. However at higher field strength, this method breaks down and the energy shifts in a non-linear way.

For strong holding fields, we can neglect the influence of the image charge and get a triangular shaped potential, which increases linear with distance. The solution to this type of potential has been found to be related to the Airy functions with the wave function being

$$\psi_n \propto \mathrm{Ai}\left(\left(z - \frac{\zeta_n}{\gamma_F}\right)\gamma_F\right) \tag{2.9}$$

with energy levels E_n and parameter γ_F

$$E_n = eE_\perp\zeta_n/\gamma_F, \quad \gamma_F = (2m_e eE_\perp/\hbar^2)^{1/3} \tag{2.10}$$

and the numbers ζ_n given by finding roots of the Airy function $\mathrm{Ai}(-\zeta_n) = 0$. This solution has been found to be accurate for higher field strength, but shows deviation due to the missing influence of the image charge term at low electric fields.

In a typical experiment conducted in this work we use intermediate holding fields, so that the image charge potential is not negligible but the Stark shift is in non-linear regime. This leads us to use a numerical solution by diagonalizing the Hamiltonian of the full

potential in (2.7) using a computer program and solving for the eigenvalues. With enough resolution, this solution is in good agreement with the analytical approaches at low and high field strength.

Of course, there are much more properties to consider about this exotic system, e.g. scattering with vapor atoms and ripplons, electron-electron interaction for different densities, in-plane mobility and transport, and importantly the formation of the Wigner solid, however a full description of these is beyond the scope of this thesis.

2.3 Qubit application of electrons on helium

Even though lots of research has been done on quantum computing, current generation computers are still in an experimental stage, suffering from short decoherence times and noisy output, as well as scaling issues. Thus, even though current state of the art computers by IBM and Google use highly developed superconductor technology, researchers and companies are looking for novel ways to build qubits. As first proposed by Platzman et al. [1], the electron on liquid helium system as described above could serve as a basis for quantum computers with high decoherence time, low noise and extremely high scalability. Specifically, they suggest a qubit based on the lowest two Rydberg levels. Electrons are deposited on a thin film of helium ($d = 0.5\,\mu$m) at very low temperatures, preferably in sub-kelvin range, where the electrons crystallize into the solid state. The electrons, which are ordered in a lattice at a constant distance $a \approx d$ from each other, can be trapped in an additional potential generated by a periodical array of electrodes, one for each electron. Individual electrons can be addressed by shifting the transition into resonance with microwave radiation. Two qubits can be allowed to interact in this manner, too, by shifting both into resonance. The readout finally occurs by making the potential barrier smaller, that electrons in excited states can escape the trapping and hit a high spacial resolution detector, which then provides an "image" of the wave function. This readout process is destructive, as it removes all excited electrons from the system. Platzman et al. calculated decoherence times of 0.1 ms and reasonable noise in the capacitor plates of 10^{-6} V.

Although this has been the first work to point out the possibility to utilize electrons on helium for quantum computing, other methods have been proposed, such as using the spin [12] or orbital states when applying a in-plane electric field [13]. Calculations have shown, that the spin-qubit can have extremely long decoherence times of up to 1×10^2 s due to weak spin-orbit coupling. Spin based qubits are also promising because of the proposed interaction method based on charge coupled devices (CCDs).

For reading out the spin states, Kawakami et al. suggested a novel method using the image charge induced by the electrons [2]. When applying an magnetic field gradient to

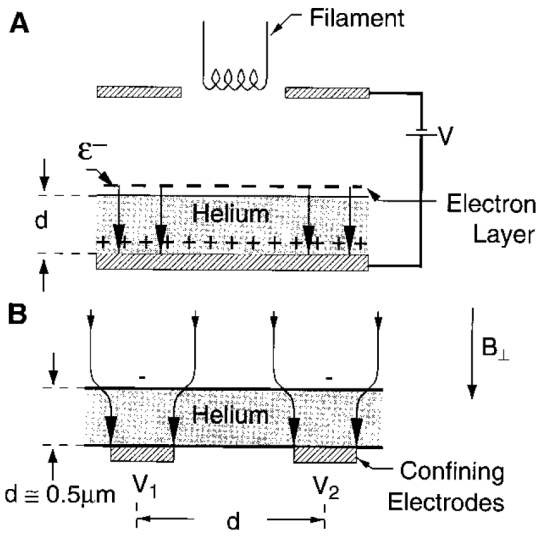

Figure 2.3: Electrode design for trapping electrons on the helium surface as proposed in the work of Platzmann et Dykman[1].

electrons in the Rydberg states, the degeneracy of the spin states will be lifted and the energy spectrum will split. The gradient ensures that the size of the energy split is different for two different Rydberg states, such that the transition frequency depends on the spin state of the electron. When applying a microwave at one of the transition frequencies and checking for a change in the image charge, one can determine the spin state of the electron. This needs very high accuracy in detecting the change of the image charge current, which has not been achieved yet [2]. Improving the sensitivity of the measurement setup is therefore paramount for a reliable readout.

3 Resonant Image Charge Detection

For the proposed spin-qubits using floating electrons, an extremely sensitive measurement device needs to be constructed, which can reliably measure, if a single electron has moved between two Rydberg states. The idea for the detection is based on detecting the change in the image charge it induces in a nearby capacitor plate. When excited, the wave function of the electron will shift away from the helium surface and the mean distance will increase, resulting in a decrease of the image charge. Let's consider an array of surface bound electrons with an areal density n_s. The difference in average distance Δz from the interface when excited from the ground state to the n-th state is then

$$\Delta z_n = z_{nn} - z_{11}. \tag{3.1}$$

For $n = 2$, this distance can be calculated to $\approx 35\,\mathrm{nm}$ (for zero pressing field $E_perp = 0$, which shift the mean distance of the Rydberg states). If a fraction ρ_{nn} of the electrons is excited to the n-th state, this will change the image charge by

$$q = \frac{\Delta z_n}{D} e n_s \rho_{nn} S \tag{3.2}$$

where S is the area of and D the distance between the capacitor plates. The changing charge will induce a current into the electrodes, which we can express as the time derivative of q. Driving this transition with a constant modulation frequency ω_m will vary the fraction of the occupancy $\rho_{nn}(t)$ periodically and generate a current signal in the electrodes, which can be conveniently detected using a lock-in amplifier. If we assume a harmonic time dependence of $\rho_{nn}(t) = \rho_{nn}\mathrm{e}^{\mathrm{i}\omega_m t}$, we can write the amplitude of the current as

$$|i(t)| = \left|\frac{dq}{dt}\right| = \frac{e n_s C_0 \omega_m \Delta z_n \rho_{nn}}{\varepsilon_0} \tag{3.3}$$

with the capacitance of the parallel plates $C_0 = \varepsilon_0 S/D$ and vacuum permittivity ε_0. Inserting some typical values $n_s = 10^8\,\mathrm{cm}^{-2}$, $C_0 \approx 1\,\mathrm{pF}$, $\omega_m/2\pi = 100\,\mathrm{kHz}$ and $\rho_{nn} = 0.1$, the current amplitude evaluates to $\approx 100\,\mathrm{pA}$, which can be easily detected with current lock-in amplifiers.

This is the image charge detection as demonstrated by Kawakami et al. [2]. However, for a single electron in the same setup ($n_s = 1\,\mathrm{cm}^{-2}$ and $\rho_{nn} = 1$), this current will only measure $\approx 0.01\,\mathrm{fA}$. In current experiments, it is not possible to resolve a signal that small

amidst the noise. We need a detection circuit, which can amplify the signal, without increasing the noise at the same time. As proposed in [2], we can attach an inductor to the cell, which forms a RLC circuit with the parallel plate capacitor of the cell. The R in this circuit is a parallel resistor, which size depends the losses in the inductor and wiring. An equivalent circuit is shown in Fig. 3.1. The electrons driven by the modulated microwaves generate a periodic current, which is connected to the cell capacitance and an inductor with an effective parallel resistance. These have the frequency ω dependant impedances $Z_C = 1/j\omega C$ with the capacitance C and $Z_L = j\omega L$ with inductance L and the imaginary unit j. Neglecting the resistance for now, we can find the total impedance of the LC circuit at the resonant frequency of ω_0 to be

$$Z = \frac{Z_L Z_C}{Z_L + Z_C} = -\frac{j\omega L}{\omega^2 LC - 1} \tag{3.4}$$

and introducing the resonant frequency $\omega_0 = 1/\sqrt{LC}$

$$Z(\omega) = \frac{1}{jC}\frac{\omega}{\omega^2 - \omega_0^2}. \tag{3.5}$$

When the frequency of the current source matches the resonant frequency, the expression will diverge to infinity. This means that the circuit will act as a band-pass filter, amplifying signals close to resonance while not affecting the rest of the spectrum. If we consider losses in the circuit due to a finite resistance of the components, only signals with a frequency of ω_0 are passing with the least attenuation (or even amplification, depending on the losses).

The question is now, what makes a good resonator for our setup? For this, we consider the quality factor Q of the coil, which quantifies the attenuation or dampening when resonating. A high Q value means an signal will oscillate longer, so there is less attenuation at every cycle. Therefore when driving a periodic current at resonance, the amplitude will be amplified more with high Q values. In an RLC circuit, the quality factor can be calculated by

$$Q = \frac{\omega L}{R_s} \tag{3.6}$$

Therefore, minimizing the series resistance of the inductor and maximizing modulation frequency as well as inductance will result in higher efficiency in the oscillation. However the inductance of the coil is usually dependent on the frequency, so increasing the frequency might decrease the inductance and cancel the benefits.

Another central concept of the resonant detection is the conversion from current to voltage, which we then subsequently amplify. According to Ohm's law $U_{\text{signal}} = RI_{\text{signal}}$, the voltage drop U over a resistor is proportional to its resistance R. This means for a image charge current of fixed size, we can generate a bigger voltage when connecting it to a big resistor. This is a reason to increase the effective parallel resistance of the inductor (as

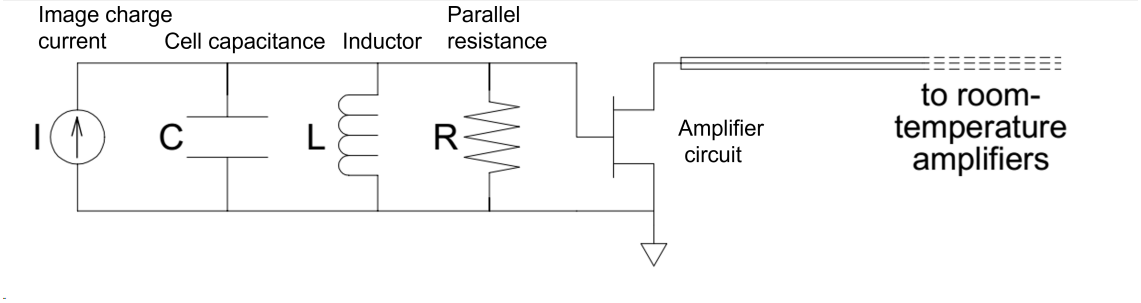

Figure 3.1: Equivalent circuit schematic of the resonant image charge detection. The current generated by the periodically excited electrons get amplified by the resonant circuit, which resonant frequency is matched with the modulation frequency to maximize amplification.

shown in Fig. 3.1) as much as possible. The parallel resistance R_p relates to these values by the expression

$$R_p = \frac{L}{R_s C} \tag{3.7}$$

therefore we need to minimize the series resistance R_s and capacitance and increase the inductance of the coil. The thermal noise voltage U_n generated by a resistance R at temperature T is known to be $V_n = \sqrt{4k_B T R B}$ with the Boltzmann constant k_B and the bandwidth B. If we consider the noise generated in the effective resistance of the resonant circuit, we find the signal to noise ratio

$$\frac{U_{\text{signal}}}{U_n} = \frac{R_p I_{\text{signal}}}{\sqrt{4k_B T R_p B}} \sim \frac{R_p}{\sqrt{R_p}} = \sqrt{R_p} \tag{3.8}$$

which means, that with increasing the effective parallel resistance, the signal to noise ratio will actually improve by the square root of the resistance. This only considers thermal noise, which has a constant spectral power density $P_{\text{noise}}/B = \text{const}$. Other sources of noise, like parasitic signals from the cell or higher temperature thermal noise transmitted through the coaxial cables are not affected by this calculation.

4 Amplifier construction

This section details the ideas and construction of the cryogenic amplifier, which took the majority of the time of the project. As made clear in the last chapter, to compensate for the high impedance of the LC circuit at resonance, a suitable cryogenic amplifier should be attached at the end of the circuit before transferring the signal to room temperature detectors. The combination of these to increase the signal to noise ratio has been used in research concerning single ion trapping for over 20 years [14, 15, 16] and was also proposed for electrons on helium [2, 17]. Additionally, attaching a second stage amplifier at a higher temperature ($\sim 4\,\mathrm{K}$) can increase the gain substantially without having problems with cooling power at the mixing chamber.

4.1 Transistor

For our application, we require an voltage amplifier with high input impedance to shunt the resonator and a very low internal noise. Additionally, since we want the amplifier mounted close to the experimental cell and reduce thermal noise in the wiring, we need a device which is operating at these criteria at sub 4 K temperatures. The power dissipation of the circuit also has to be considered, since the dilution refrigerator has very limited cooling power at low temperatures.

Reviewing the literature, research groups in single ion trapping have been using Gallium Arsenite (GaAs) transistors for over 20 years [14, 15], although the detection for ions operates at higher frequencies (64 - 200 MHz instead of 1 kHz). Finding a suitable transistor is not trivial, since their characteristics differ greatly when cooled to sub 4 K temperatures. A single-gate circuit design with a High Electron Mobility Transistor (HEMT) has been found to be very useful to the group [14]. HEMTs were invented in 1979 in Fujitsu labs and have replaced MESFETs in satellite receivers because of their superior noise characteristics. Since then, HEMTs have been used in cryogenic applications, e.g. in low-noise radio astronomy detectors. An additional feature is that HEMTs can be operated at much lower power than intended, while maintaining good noise performance and high gain.

In particular, we settled on a design based on the Fujitsu FHX13LG transistor, which is intended for RF frequency applications, but has been used successfully by [14] for frequencies between 64 and 200 MHz. Before constructing the amplifier board, we performed gate and drain voltage sweeps to check the operation of the transistor at room temperature as

well as 200 mK. The low temperature measurements are important, since characteristics of the transistor can change drastically. We perform a sweep of the gate voltage V_G, and drain voltage V_D while measuring drain current I_D. Fig. 4.1 shows the measurements and calculations. We see an increase in source-drain current, when applying higher voltages to the gate and drain ports (top left image). From this data, we can calculate the output resistance R_D, which is given by

$$R_D = \left(\frac{dI_D}{dV_D}|_{V_G} \right)^{-1} \tag{4.1}$$

Higher output resistance can lead to higher gain, but it usually has to be matched to the transmission line at 50 Ω to prevent reflection. We can also calculate the transconductance g_m between gate and drain by the slope

$$g_m = \frac{dI_D}{dV_G}|_{V_D} \tag{4.2}$$

which is related to the gain of the transistor (shown in bottom left). As expected, the gain is higher for higher output current as seen from the top left image. Since we are also interested in low power dissipation, we try to find the highest transconductance for the lowest power output. By multiplying the drain-source voltage V_D with the measured current I_D, we calculate the dissipated power at the transistor $P_{\text{diss}} = I_D V_D$. We calibrate this to an approximate temperature by powering a heater mounted inside of the fridge (with a resistance of $R_{\text{heater}} \approx 100\,\Omega$ with various currents and checking the settling temperature. By a linear least-squares fit, we can determine a coefficient between output power and temperature. Fig. 4.1 bottom right shows a filled contour of the transconductance with isothermals as calculated from the total output power from the transistor. We can clearly identify a higher transconductance at lower (more negative) gate voltage and higher drain voltage while staying at the same temperature. For higher efficiency, we will operate the amplifier in this region.

4.2 Amplifier circuit

After confirming correct operation of the transistor, we incorporated it into an amplifier design adapted from [14]. The fundamental schematic of the amplifier circuit it shown in Fig. 4.2. The trap input wire is connected to the experimental cell and is coupled capacitively to the input of the transistor. Connected to it is the inductor (shown without a value), for which we use a specifically designed coil as described later. The signal output is connected to a coaxial cable leading to the second stage amplifier. Parallel inductor and resistor at the drain of the transistor act as a attenuator for high frequencies, which prevents excess feedback and improves the stability of the amplifier [14]. Gate biasing

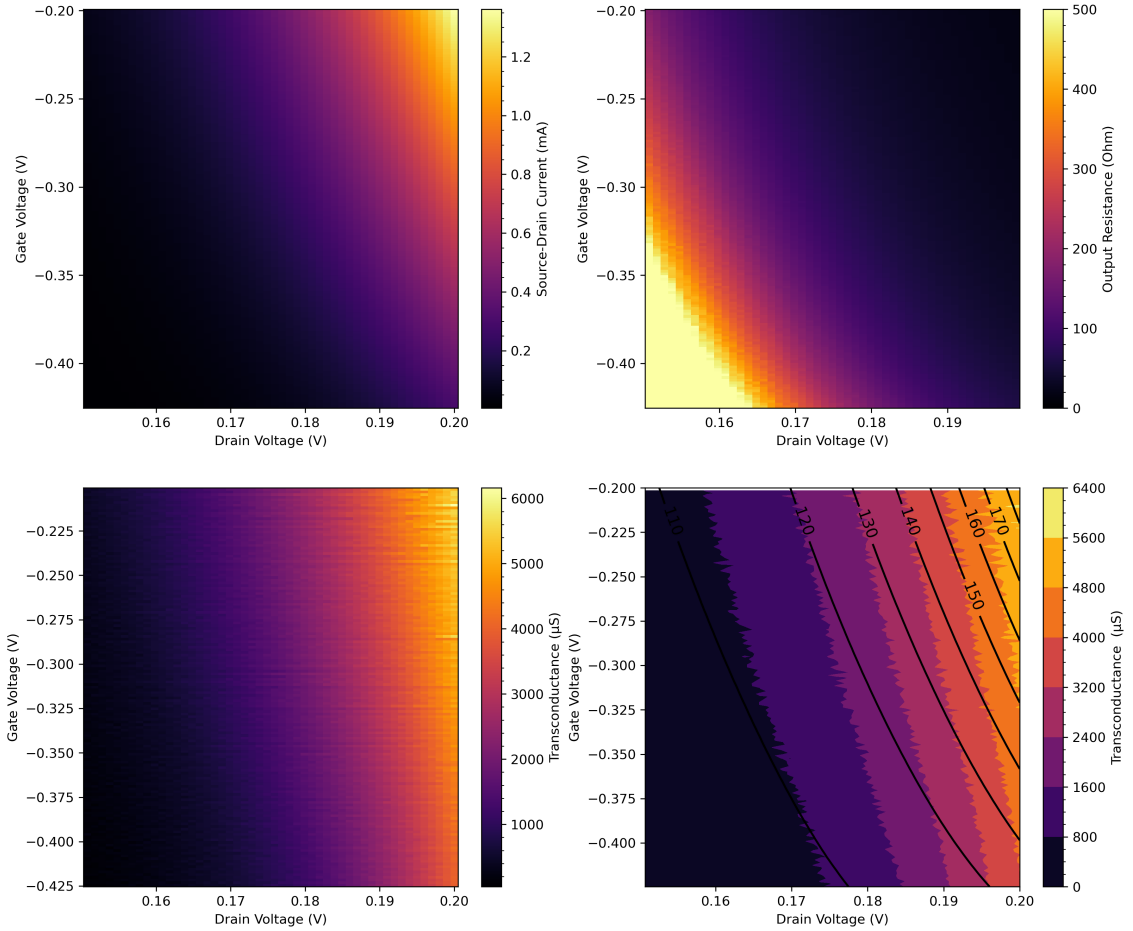

Figure 4.1: Measurements of the transistor at $T = 200\,\mathrm{mK}$. (top left) Source-Drain current as measured when applying biasing voltages to gate and drain. (top right) DC output resistance calculated from the data. (bottom left) Calculated transconductance between gate and drain. (bottom right) Transconductance with overlayed isotherms for estimated temperature calculated from the power dissipation in Millikelvin. The high (negative) gate biasing region gives a higher transconductance for the same power dissipation.

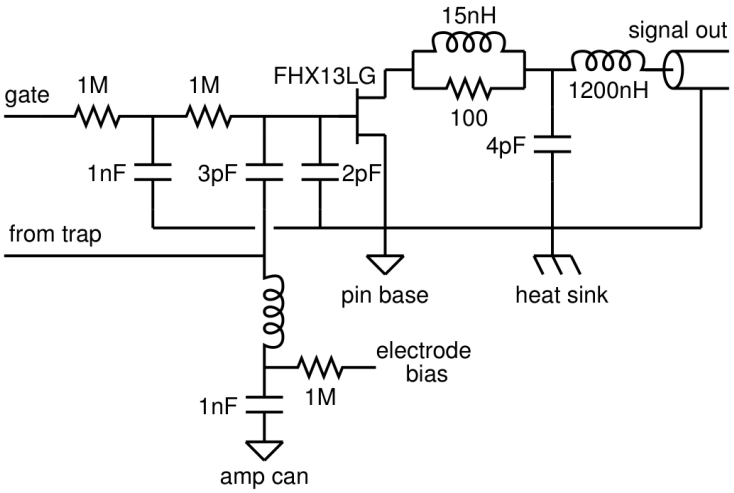

Figure 4.2: Schematic of the amplifier circuit used by D'Urso et al. [14] and very similar in [15]. To adjust the impedance matching circuit on the output port to the lower frequency, the capacitor and coil were adjusted to 680 pF and 22 μH. Figure reproduced from [14].

is enabled directly through a connector on the amplifier housing, while the bias for the electrode has to be connected to the far end of the coil, outside of the amplifier. This is not an issue, since for dc voltages, the inductor behaves like a simple resistor. The biasing of the drain of the transistor is enabled only by connecting a bias-tee to the output coaxial cable. The DC biasing voltages are decoupled from the ground by inserting capacitors appropiately.

Since the original circuit was designed for detection of ions at a frequency of 64 MHz, the impedance matching circuit (inductor and capacitor connected to the output cable) has to be adjusted. For matching the 50 Ω coaxial cable, we inserted a capacitor with 680 pF and a inductor with 22 μH.

4.3 Construction and mounting in the fridge

To uphold high performance characteristics of the tank circuit, we have to take a few key points into consideration. The amplifier should be mounted as close to the cell (capacitor) and coil as possible. This reduces stray capacitance from connecting coaxial cables, which improves the quality factor of the resonator. This required constructing a mounting mechanism to attach the coil and amplifier directly to the connector on the cell. Another very important consideration when putting this design onto a physical PCB is the heat sinking of the transistor, since we want to keep the temperature of the amplifier circuit low to reduce thermal noise as much as possible. It was therefore practical to build a thermally conductive housing for the amplifier, with one of the source leads of the transistor soldered directly to it. Fig. 4.3 shows the circuit board inside of the machine milled copper housing.

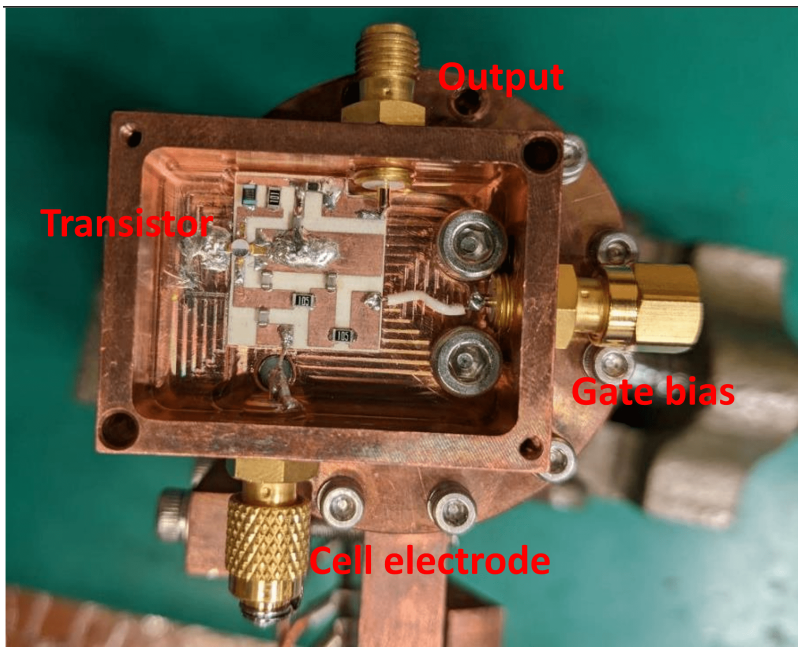

Figure 4.3: Circuit board in the housing. Case made of pure copper, with a wall thickness of 3 mm. The source lead of the transistor is soldered using a low temperature indium based solder onto the copper housing

The PCB is made from Rogers RO4000 material, which is designed for RF applications. After all components were soldered to the board, the PCB is fixed onto the standoff in the housing and the transistor soldered to the pads and copper housing using a indium based low temperature solder. We opted for a low temperature solder since traditional solder requires temperatures at which the transistor might be overheated.

We then designed a mounting mechanism, to fix the amplifier and coil as close to the cell as possible. The adjustable arm is made of solid pieces of copper with multiple joints. The whole contraption is shown in Fig. 4.4. The coil shield cover has a hole, through which a short coaxial cable connects the circuit with the coil windings. The biasing port is supplied on the back side of the coil (not shown).

For the inductor, we used a helical resonator design, also used widely in e.g. [14]. Specifically, we use a Niobium Titanium wire (superconducting below 4 K) wrapped around a PTFE core and mounted in a copper shielding with a thickness of 3 mm. Measurements at room temperature determined the parallel resistance to be 355 kΩ, which is much less than the measured 2.6 MΩ later determined in the experiment. The quality factor Q was measured by the 3dB method to $Q \approx 1552$ by connecting it to a vector network analyzer. The added capacitance and circuitry when mounted in the experiment decreased this to 300-400 (depending on the amount of deposited electron in the cell, which affects its capacitance).

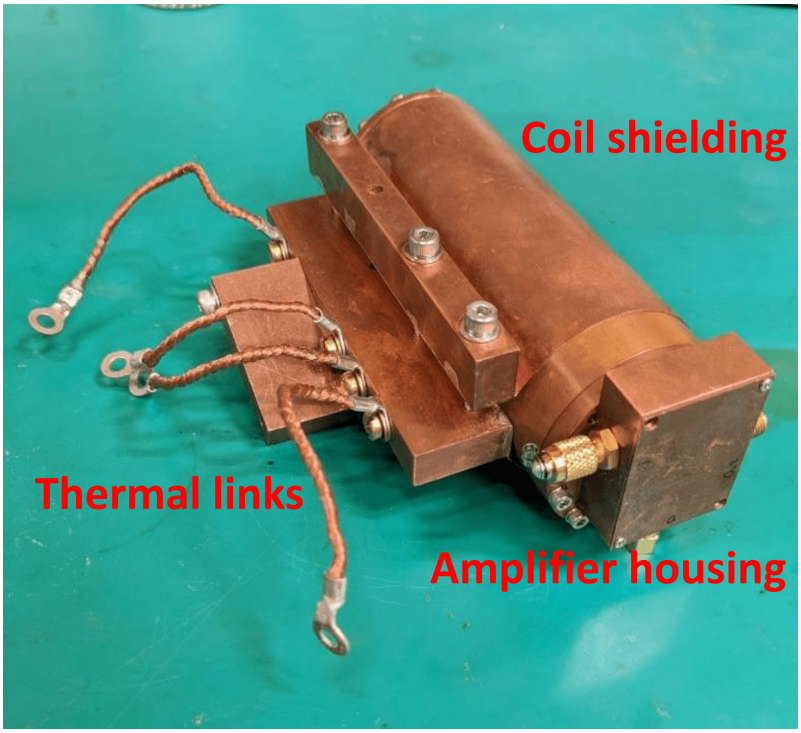

Figure 4.4: Amplifier housing connected to the coil and mounting contraption. The parts are made of pure copper, with the coil consisting of a NbTi wire wrapped around a PTFE core.

5 Corbino Disc Experiment

To test the constructed amplifier, we analyze its properties in a real experiment at low temperatures. Using a cell which contains a parallel plate capacitor, we can trap electrons on bulk liquid helium and read out their image charge signal using the electrodes, which are connected directly to our amplifier. This approach allows us to test the noise performance of the amplifier with actual surface bound electrons in a setup very similar to the more delicate micro-channel devices. We also demonstrate Rydberg excitation of the electrons and calculate various properties of the amplifier from the measurements.

5.1 Experimental Setup

5.1.1 Dilution fridge

Since helium will turn liquid only below 4.15 K, we require a system that can sustain a sufficiently low temperature for the duration of our experiments. It is preferable to operate in sub 1 K temperatures to reduce thermal excitation of the electrons and reduce scattering rate. For cooling down to such a low temperature, we need a ^{3}He evaporation fridge. A dilution refrigerator (DR) offers high cooling power at low temperatures and continuous operation and is widely used in the quantum computing field [18]. For this experiment we use a BlueFors LD-400 dry (cryogen-free) DR system. The working principle is briefly reviewed.

The cool-down process takes place in two steps: The pulse tube pre-cooling and the ^{3}He-^{4}He condensation and circulation. After pumping the vacuum can to achieve a good thermal isolation, the pulse tube is engaged. The first stages cold head is connected to the 50 K flange, the second stage to the 4 K flange, which is roughly the temperature it is able to cool down to. This is low enough for ^{4}He to liquefy and thus start the condensation of the mixture.

Fig. 5.1 shows a schematic of the cooling mechanism. The ^{3}He and ^{4}He mixture is compressed and introduced to the DR lines, where it condenses. Once the mixing chamber (MC) and part of the still have filled up, the circulation can be started by pumping the still. Since the vapor will be pumped away first, it is replaced by evaporation of the liquid phase, which removes thermal energy and cools the MC down to roughly 0.8 K. The mixture in the MC will now separate into a ^{3}He-rich and ^{3}He-poor phase, where the ^{3}He-poor phase

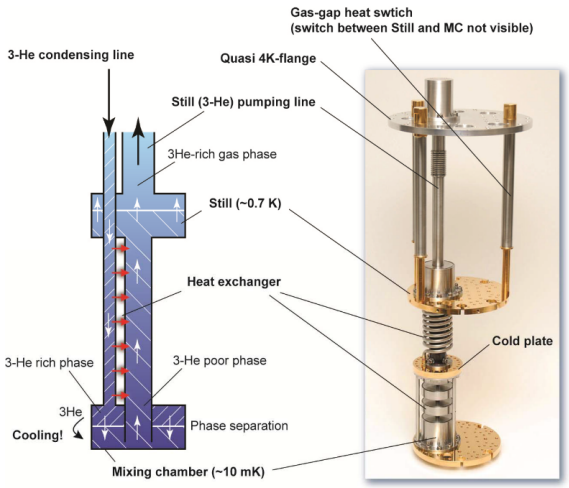

Figure 5.1: Schematic of the BlueFors dilution refrigerator apparatus. Image reproduced from the manual.

sinks to the bottom due to the heavier ^{4}He atoms. The ^{3}He will now circulate through this mixture through the osmotic pressure difference, resulting in additional cooling, reaching to temperatures as low as 10 mK. In our experiments, the temperature of the cell mounted on the MC plate is much higher (100-200 mK) due to the dissipation of the amplifier and heating of the electrons by the microwaves. More about the working principle of the DR can be found on the manufacturers website[1]and the manual.

5.1.2 Experimental cell

To confine electrons on a helium surface, we use a cell which contains a parallel plate capacitor with a corbino disc structure, which has three electrodes on the bottom and top part, as seen in Fig. 5.2. The electrodes are labeled as center, middle and guard for the top (TC, TM, TG) and bottom (BC, BM, BG). The center and middle electrodes will be used for measurements, while the guard is biased negatively during most experiments to create a potential barrier to confine the electrons. The cell containing the capacitor is made of copper (a good thermal conductor) and is sealed airtight using an indium gasket. It features eight electrical connectors (SMP), an entry port for the wave guide and one helium filling line. It also contains a tungsten filament, which is used to deposit electrons on the helium by thermionic emission.

An import design goal was to mount the resonant circuit as close to the cell as possible to reduce stray capacitance and maximize the quality factor. Because of this, the amplifier is mounted on the coil shielding and connected directly to the BC port on the cell (see Fig. 5.3). This also minimized thermal noise generated by the resistance of wires as well as

[1]Link to the company website as of time of writing: `https://bluefors.com/products/ld-dilution-refrigerator/`

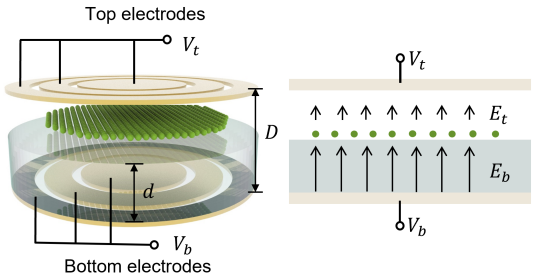

Figure 5.2: Schematic of the inside of the experimental cell. Electrons (green spheres) float atop the helium liquid and are held by an attractive potential on the bottom center electrode, as well as a repulsive potential on the outermost bottom electrode. In our setup, electrodes are not connected and can be individually biased. Image reproduced from [4].

capacitance affecting the circuitry of the amplifier.

A wiring diagram of the experimental setup is shown in Fig. 5.4. The experimental cell is mounted on the mixing chamber plate for thermal connection, which reaches a temperature of less than 100 mK in our experiments. The electrodes of the corbino disc can be individually biased and driven with an AC voltage through a bias tee. To generate pulsed bursts of microwaves, the output of a high-frequency signal generator (1-20 GHz) is modulated by a pulse wave with a frequency f_0 supplied by a waveform generator (AWG). The signal is attenuated and its frequency multiplied by 12 times to achieve frequencies in the range of the Rydberg transition of the electrons. The waves are guided to the experimental cell through a thermalized, rectangular stainless steel waveguide. As seen in the schematic, the BC is connected to the amplifier chain with the lock-in detector at the end, which is used to detect the amplified voltage signal from the image charge current at the modulation frequency f_0. The reference signal is provided by the waveform generator (AWG) and is locked to the same frequency as the modulation signal to the microwave generator. A second lock-in is connected to TC with its internal oscillator driving an AC current to the TM. This is a so called Sommer-Tanner measurement [8], which is used to estimate the electron density on the surface. Since the electrons are highly mobile in the horizontal, the capacitive coupling between the reference and the pick up will increase with more electrons on the surface. This is a good measurement to check, if electrons are deposited during the experiment. Furthermore we connect two lines in the mixing chamber and estimate the attenuation of the wires using a network analyzer.

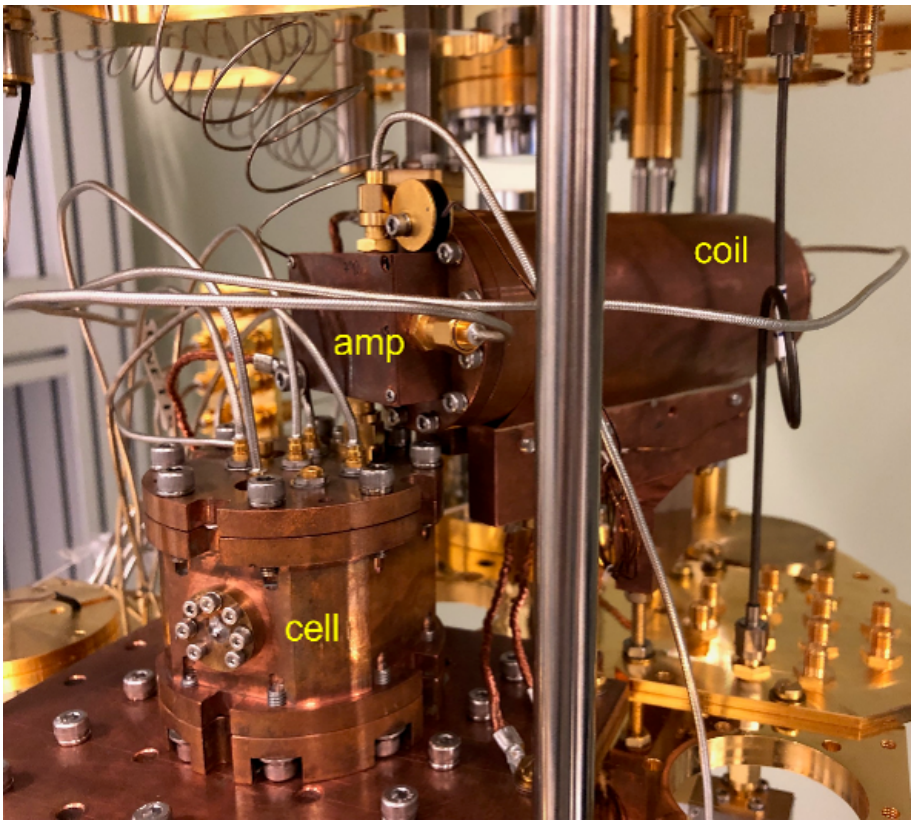

Figure 5.3: Setup of the cell, coil and amplifier in the fridge before cool down. The amplifier housing is connected to the coil and thermally linked to the MC plate (at the bottom of the picture). Connection length between read-out electrode and amplifier input is kept to a minimum by directly connecting amp to the cell with a SMP connector.

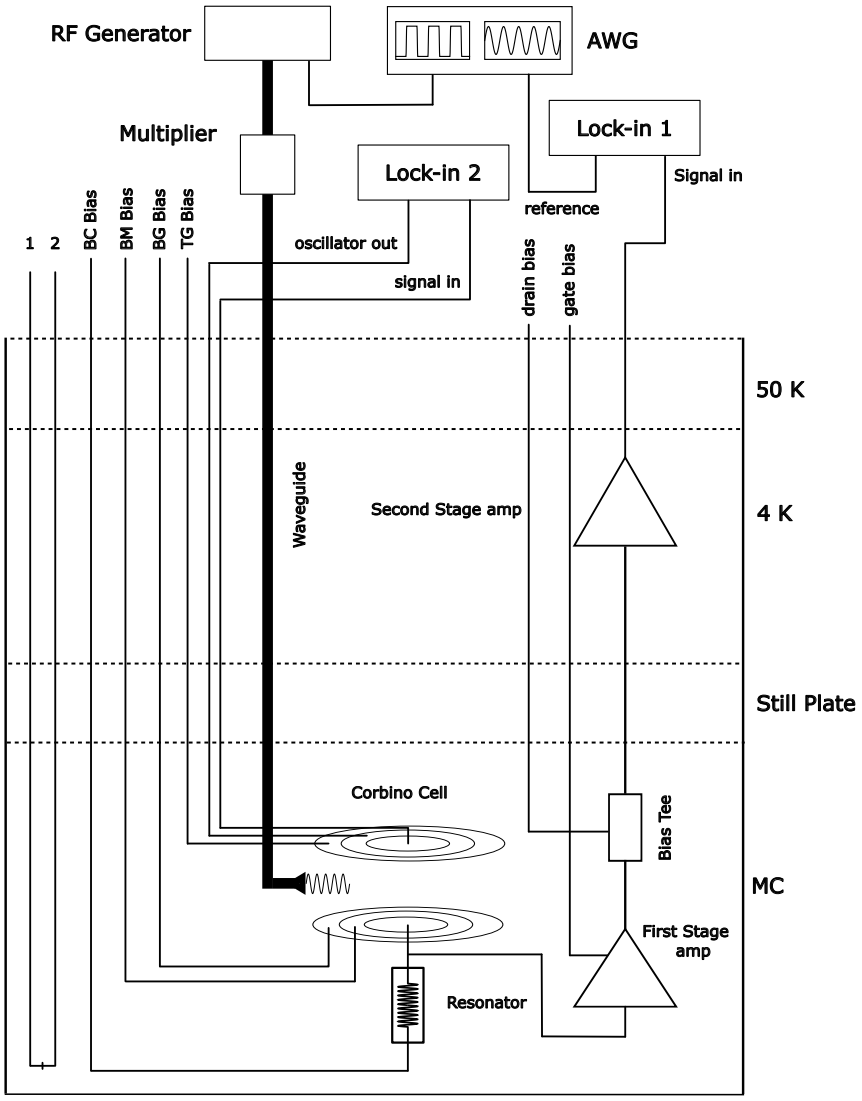

Figure 5.4: Schematic and wiring diagram of the experiment setup. Electrodes of the corbino disc can be independently biased with DC voltage and driven with an AC voltage over bias tee. Lines 1 and 2 are identical to all other coaxial lines, but are connected at the MC to check the attenuation of the wires. The components are thermally linked to the corresponding section of the fridge as indicated on the right side. For wiring, we use coaxial cables with a grounded shielding. For the biasing lines we use ecosorb microcoax cables with $-30\,\mathrm{dB}$ attenuation above $50\,\mathrm{MHz}$.

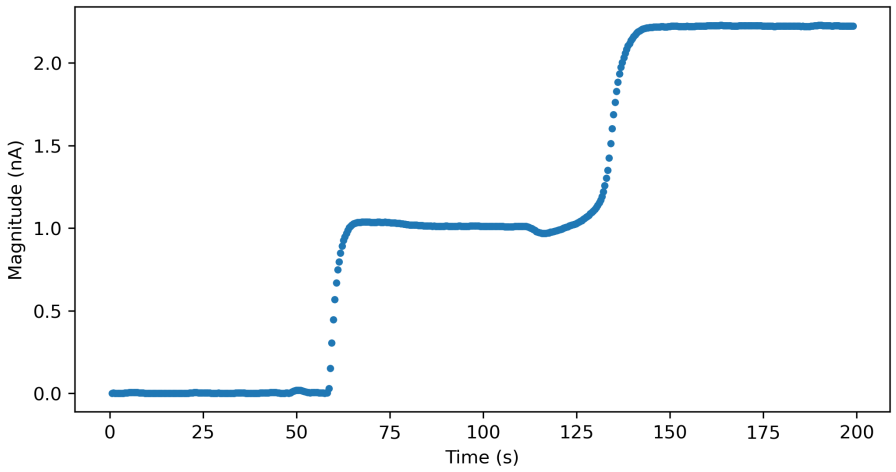

Figure 5.5: Deposition process for filament voltage −3.2 V and BC and BM bias of 3 V. Signal measured using Sommer-Tanner method at BC and BM electrodes. Ramping of the guard electrode pushes electrons to the center of the disc and increases electron density significantly.

5.2 Preparation of the electrons

After a complete cool-down of the fridge to a base temperature of approximately 120 mK at the MC, ^{4}He is filled into the cell until its surface is half the height of the capacitor plates. To prevent the temperature rising too much, the condensation is performed slowly. A practical way to measure the filling level is to calculate the change in capacitance between two facing electrodes due to the different permittivity of helium of $\varepsilon = 1.056$. Then the capacitance at half-filled is

$$C_{50/50} = C_0 \frac{2\varepsilon}{1+\varepsilon} \tag{5.1}$$

Electrons are deposited by applying a voltage of about 3.2 V with 13 mA of current to the filament for a few seconds. The deposited electrons are held by the attractive potential on the bottom inner and middle electrode and prevented from exiting the disc by a potential barrier at the guard electrode. In Fig. 5.5 a transient Sommer-Tanner measurement between TM and TC is shown. The initial burst of electrons result in a current increase of about 1 nA. The signal increases again significantly by biasing the guard electrode to a negative voltage to push electrons into the center of the disc. Once deposited, electrons stay on the helium surface for several days if not disturbed; thus it is reasonable to assume that during measurements, the electron density does not change significantly and does not effect the measured Rydberg signals.

5.3 Operating point of the amplifier

Since the amplifier is an active component in the circuit, we have to supply power for it to function. The performance can be tweaked by applying a biasing voltage at two different points: the gate of the transistor and at its drain (cf. electronic schematic in Fig. 4.2). To find the optimal working point, we are looking to maximize the amplification and, even more importantly, the signal to noise ratio of the output while keeping the power dissipation low enough to not overheat the setup. At higher drain voltages, we expect to see improved gain with the drawback of added power dissipation. Increased power may also increase the noise added to the signal by the operation of the transistor, as well as higher thermal noise.

Sweeping both gate and drain voltage while measuring the amplified reference signal yields Fig. 5.6 (top). For a moderate gate bias (roughly $-3.5\,\mathrm{V}$) and maximum drain voltage (limited to $0.3\,\mathrm{V}$ to prevent excess heating) we can clearly see the highest signal. The voltage noise coming from the experimental cell can be estimated by running the same measurement without the reference signal as seen in Fig. 5.6 (middle). From this data, we can calculate the signal to noise ratio (SNR) at the end of our amplification chain as shown in Fig. 5.6 (bottom). For every step of the gate voltage, the SNR saturates at roughly 6, even when driving more drain current. This tells us, that the SNR in this region is not limited by the first stage, but rather the second amplifier. Driving more current at gate voltage $-3.5\,\mathrm{V}$ however also increases power dissipation. Therefore we choose a slightly more negative gate bias voltage of $V_{\mathrm{gate}} = -0.437\,\mathrm{V}$ for future operation, where we reach the saturated SNR of about 5-6 with the lowest possible power input.

5.4 Rydberg transition

Since we have found a set of biasing values to operate the amplifier, now we try to observe the dependence of the Rydberg transition frequency on the pressing field exerted by a voltage bias on the BC electrode. Due to the Stark effect, the energy of the Rydberg states are spread out, which results in a shift in the transition frequency. The field is generated by applying a biasing voltage to the BC electrode through a bias-tee. For simplicity's sake, we consider only the field from the electrode, even though there is a minor contribution by the image charge induced into the electrodes by the electrons. However this effect is very small when the helium filling level is close to half the distance of the capacitor plates, since the opposing image charges will cancel out if spaced at equal distance (see Chap. 1.2.2 [4]).

In Fig. 5.7 we show the data for this experiment. For a range of biasing voltages[2] we sweep the microwave frequency to find the resonance in the lock-in signal. The resonance is visible in both R (left) as a strong signal, and in the phase (right) as a coherent phase relation to the reference signal in the vicinity of the resonance. We observe a dominant

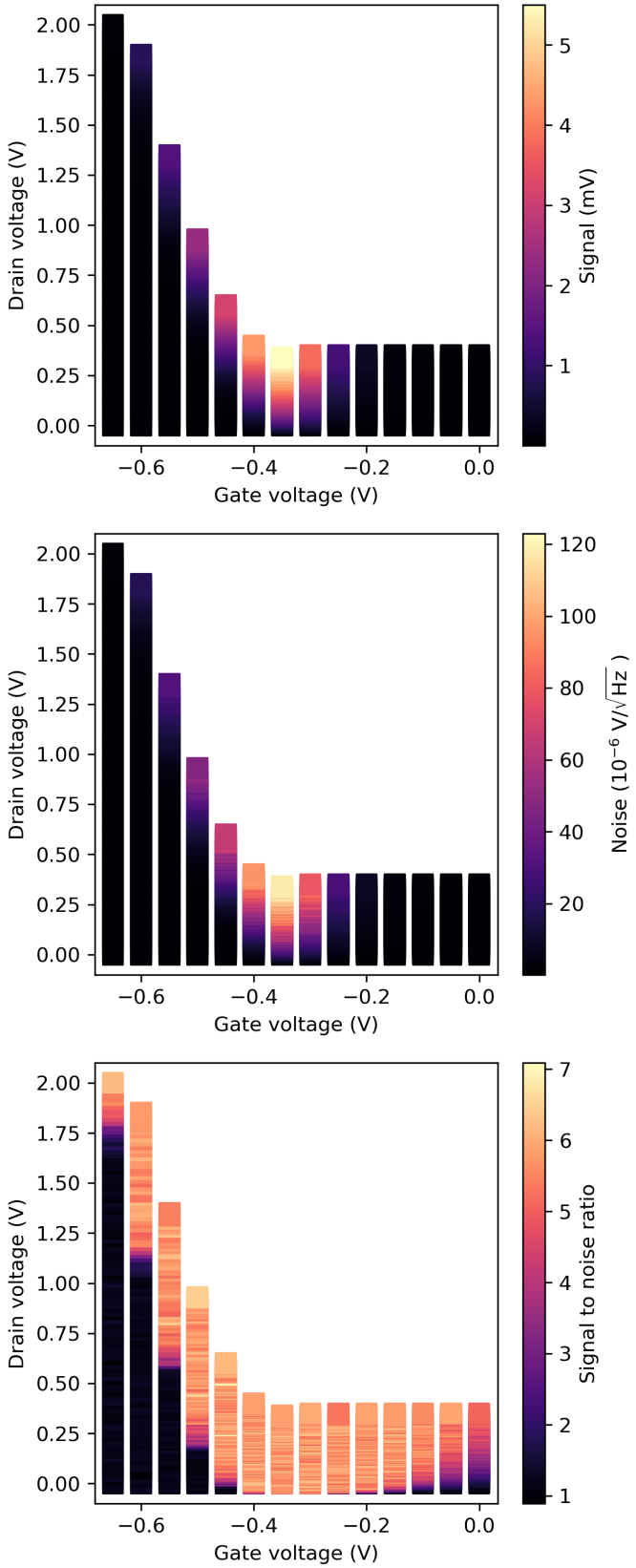

Figure 5.6: Gate and drain biasing voltage sweep for resonant microwave excitation. To prevent excess heating of the cell, the upper limit of the drain bias is limited to 0.35 V for lower gate bias. The R component of the lock-in (top), the noise density (middle) were measured and the SNR calculated from these measurements for a bandwidth of 1 Hz.

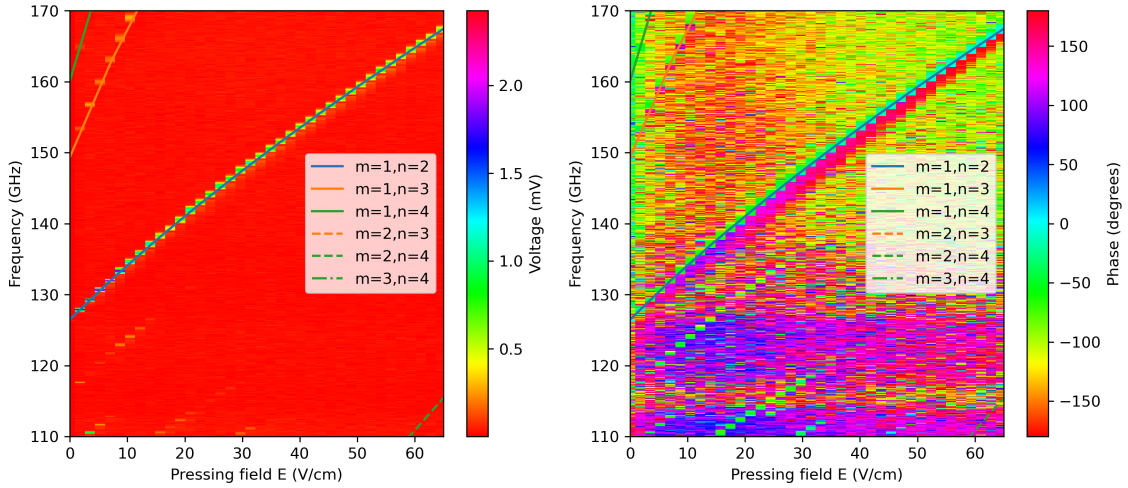

Figure 5.7: Rydberg resonance in the lock-in measurement over microwave frequency and the pressing electric field (calculated from the bias voltage at the BC electrode). Shown left is the R component and right the phase of lock-in signal. Next to the dominant transition across the diagonal there are more, less strong transitions. The line plots are the numerical solution for select transitions. Some calculated transitions are not visible in the scope of the experimental data.

transition across the diagonal, as well as some less intense transitions. From the frequency at the lowest biasing voltage of about 126.6 GHz, we can identify the dominant transition with the 2-1 Rydberg transition. Furthermore we can see from these image, that the Stark effect increases the frequency of the transition in this experimental region at moderate pressing field, meaning the difference in energy of the Rydberg states is increasing.

To validate the results and find the origin of the other resonances, we compare the data to a numerical solution of the system. The one-dimensional Hamiltonian as described in (2.7) of a single electron floating on helium with an electric field can be diagonalized to find the energy of the Rydberg states. For this model, we assume a potential barrier of 1 eV (which has been found to align with experimental findings) at the helium surface and convert the biasing voltage from the experimental data to the electric field in the center of a parallel plate capacitor by the formula $E = U/d$ with $d = 1.91$ to fit the model to the data. The calculated transitions are plotted over the experimental data in Fig. 5.7.

We can see, that the 2-1 transition matches very well with the experimental data. We can also identify the 3-1 and 4-1 transitions at the top left of the image, as well as the 4-3 at the bottom right, which also appear in the experimental data. However, resonance lines with the same slope as the 2-1 transition at lower frequency are not explained by the model (also not by any other transition of higher order). The cause of these signals is not clear, however we suspect, that the actual potential $V(z)$ has in fact another area of stable states,

[2] In the Figure, the biasing voltage was converted to approximate pressing field for easier comparison with the theoretical model as explained a bit later.

which results from the fact that electrons are discrete point sources of the electric field. A quick simulation showed that this additional potential well is approximately harmonic, which explains the equally spaced additional lines.

5.5 Detection sensitivity

As explained before, we try to achieve a higher image charge sensitivity by using a resonant circuit coupled with the low-temperature pre-amplifier. In theory, we describe our sensitivity to electrons by the amount of voltage signal $U_{\text{lock-in}}$ we measure at the lock-in amplifier in relation to the actual image-charge current I_{ImCh} generated by the electrons. In a typical corbino disc experiment, this current for a single electron on the 2-1 transition measures $\sim 0.02\,\text{fA}$, although it is much higher for micro-channel devices [19], since the distance to the electrodes is much smaller. The amplified image-charge signal is picked up through BC, while we measure the direct current from TC (lock-in frequency tuned to the modulation frequency of the microwave generator). We operate the amplifier at $V_{\text{gate}} = -0.437\,\text{V}$ and $V_{\text{drain}} = 0.25\,\text{V}$.

Shown in Fig. 5.8 is the amplified signal from the BC electrode over the microwave frequency at a modulation frequency in resonance with the LC circuit $\nu = 1.226\,\text{MHz}$. Due to the biasing of the electrode, the Rydberg resonance is shifted to 130.7 GHz. The signal to noise (average background signal) equals 34 dB (49 linear SNR). In comparison, Fig. 5.9 shows the signal from TC without amplification. The modulation frequency is shifted out of resonance to $\nu = 1.4\,\text{MHz}$ to bypass any amplification from the resonant circuit, since it is coupled through the capacitance of the cell. The Rydberg resonance is easily identified at a similar central frequency. The blue line is drawn by calculated a moving average to highlight the resonance amid the noise. We see a signal peak which is 4.28 pA higher than background. From this, we can estimate the smallest detectable signal, which is a signal with a SNR ≥ 1. Dividing the direct current by our SNR of the amplifier circuit yields a minimum detectable current of 87 fA.

In previous experiments with micro-channel devices, the image charge current induced by a single electron was measured to 4.9 fA; therefore we can estimate amplification chain to be able to detect the image charge signal from as few as 18 electrons on the helium surface in a micro-channel device. Methods for improving the sensitivity will be discussed later.

We can also calculate the voltage gain of the amplification chain (including the attenuation of the wires), which is the ratio of the voltages at the input of the transistor and output of the second stage. Driving the direct current across the resonator with an effective resistance of $2.6\,\text{M}\Omega$ yields a voltage of $11.12\,\mu\text{V}$, which is divided by the capacitors by

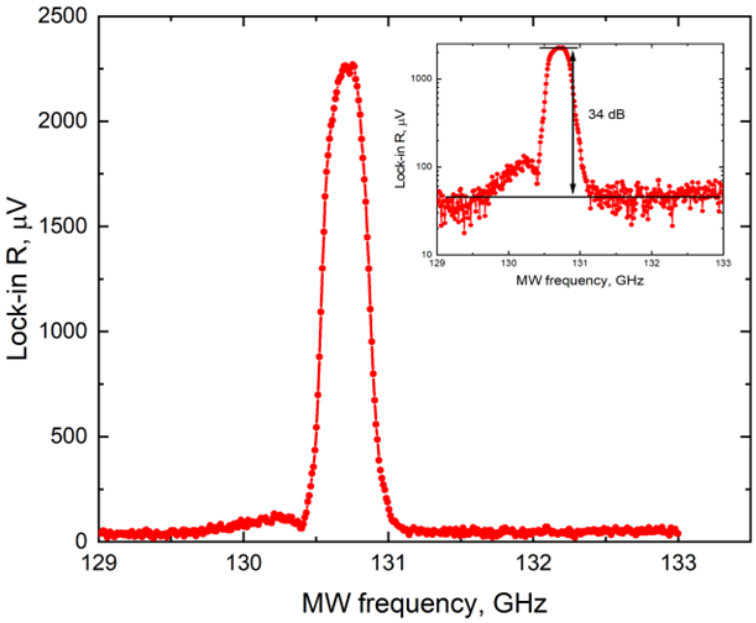

Figure 5.8: Image Charge current from electrons on bulk helium, read out and amplified by the resonant circuit from BC. Lock-in time constant $\tau_c = 1$s, slope 12dB at bandwidth 0.125 Hz. The small figure shows logarithmic display of the graph. The signal to noise ratio of the resonance peak to the average background is 34dB.

$3\,\mathrm{pF}/2 + 3\,\mathrm{pF} = 0.6$. Compared to the signal in Fig. 5.8 we compute

$$\frac{2151\,\mu\mathrm{V}}{6.67\,\mu\mathrm{V}} \approx 322.$$

According to the data sheet of the FHX13LG, it has typical associated gain of 13 dB ≈ 4.4 (for room temperature), with increasing tendency towards lower temperatures. Coupled with a gain from the second stage amplifier of 35-45 dB ($\approx$ 55-170) (since the amplifier is designed for higher frequencies, the actual amplification is difficult to infer from the data sheet alone), this result aligns with the proposed gain of the amplifiers.

To further reduce noise and improve sensitivity, we can tune the lock-in parameters time constant τ_c and slope of the filter, which affect the bandwidth of the integrated frequency range. As discussed before, reducing this bandwidth after transforming the spectrum results in less noise being integrated with the signal and generally leads to an improvement of the SNR. This comes at the cost of increased time until the reading has settled to the actual value, which can increase to several seconds or minutes. For the purpose of characterizing the performance of the system this is not an issue.

For all available combinations of τ_c and slope, we measure the signal for resonant microwave excitation, non-resonant excitation and disabled microwave radiation while having electrons deposited on the helium surface. The result is shown in Fig. 5.10. The

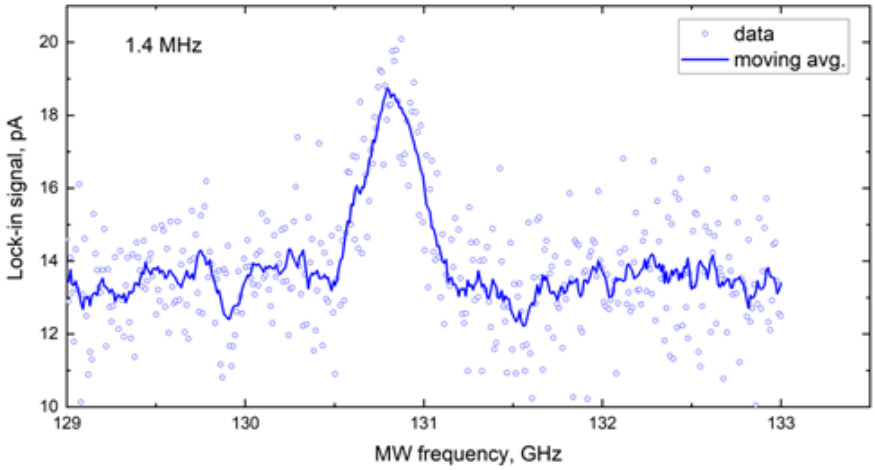

Figure 5.9: Direct measurement of electrons on bulk helium using TC electrode without any additional amplification. Lock-in time constant $\tau_c = 1\,\mathrm{s}$, slope 12dB at bandwidth 0.125 Hz. Blue line is a moving average over neighboring data points. The modulation frequency is shifted away from the resonant frequency to 1.4 MHz in order to prevent coupling through the cell to the inductor.

signal of the resonant excitation is close to our previous measurement and approximately constant over the bandwidth. This is due to the parasitic signal having a bandwidth much narrower than the lock-in bandwidth. This also holds true for the non-resonant microwaves, even though the signal is much weaker. However when the microwaves are turned off, this results in a further drop of the noise floor, which shows a linear dependence on bandwidth B in the log-log plot. A linear representation shows a trace with a $\sqrt{B}$ dependence. This hints at the presence of white noise, which spectral power density is constant and thus increases linearly in power (square root in terms of voltage).

This poses the question where off-resonant signal comes from, since it is clearly not dependent on the lock-in bandwidth and we find the white noise only when turning the microwaves off completely. Using a spectrum analyzer, we measure the amplified signal over a 1 kHz span around the tank circuit resonant frequency. Fig. 5.11 shows the signal for resonant, off-resonance and disabled microwave radiation. With resonant excitation, a SNR of 40.9 dB is observed. However, when shifting the microwave frequency away from resonance, a signal at the resonant frequency with a considerable SNR of 8.1 dB remains, which gives us the actual SNR of $\approx 34\,\mathrm{dB}$. The signal disappears when the radiation is disabled. Since this signal is very narrow, it is not affected by changing the bandwidth of the lock-in. The presence of the parasitic signal reduces our actual SNR performance since it is indistinguishable from the the electron signal at resonance.

In conclusion, in this chapter we have demonstrated that the amplifier is working and can be operated efficiently without excessively heating the MC. Furthermore we calculated a SNR of 34 dB, with which we can potentially detect as few as 18 electrons. A parasitic

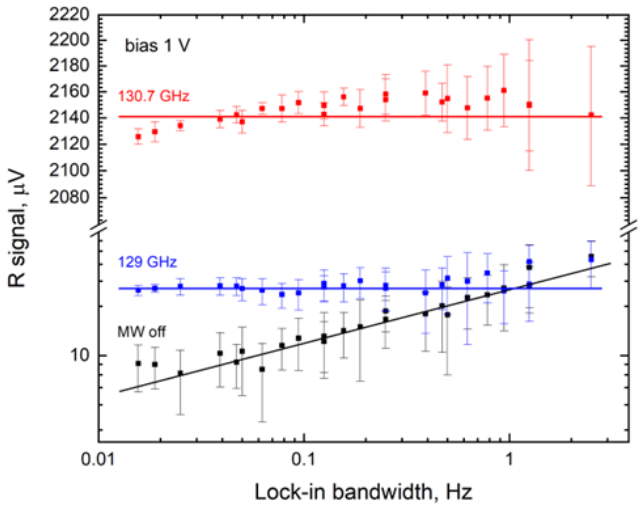

Figure 5.10: R component of the lock-in amplifier as a function of bandwidth by tuning of the time constant τ_c and the order of the low-pass filter. The measurement was repeated with the same parameters for resonant microwaves at 130.7 GHz, off-resonance at 129 GHz and with disabled microwave generator.

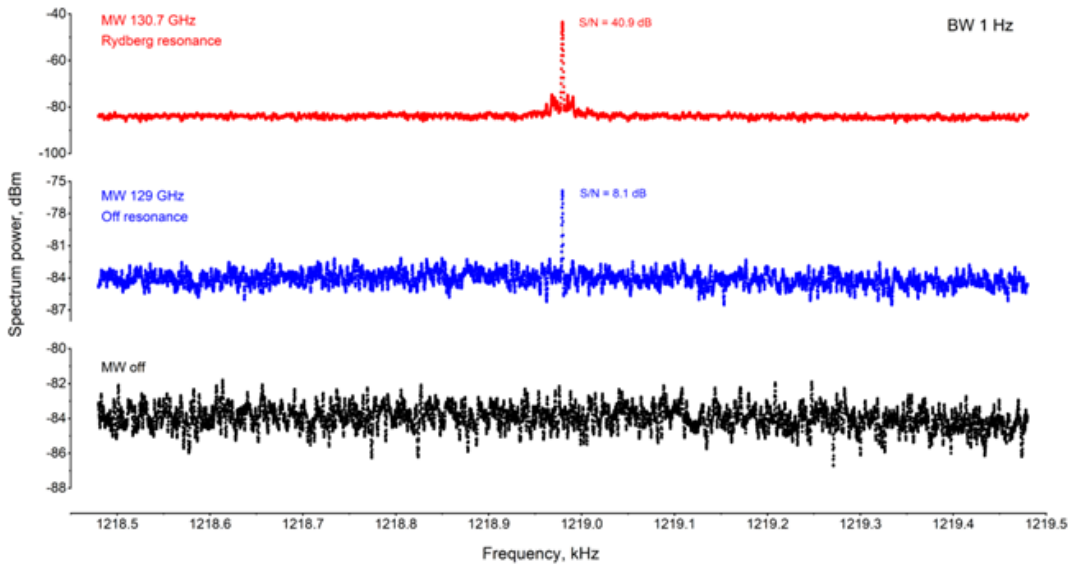

Figure 5.11: Image charge signal measured by a spectrum analyzer connected to the amplifier chain. The frequency range is limited to a very narrow sweep at the top of the resonance from the tank circuit.

signal, which appears when engaging microwave radiation, is limiting the performance of the amplifier. The origin of this signal has to be eliminated before we try to tune the parameters of the amplifier for better performance.

6 Conclusion

In summary, in this work we have developed a detection device suitable for ultra low noise readout of the image charge signal and demonstrated its performance in a low temperature experiment. The cryogenic amplification coupled with the resonating circuit gives a SNR of 34 dB, which is limited however by the appearance of a parasitic signal with very narrow bandwidth. The minimum detectable signal when performing experiments in a micro channel device was calculated to 18 electrons, which is only one order of magnitude above the signal of a single electron. When achieving single electron readout, the experiment can be modified to include a magnetic field gradient, which makes the transition frequency spin dependent. Thus, if a change in the state is detected, the spin state can be read out in a non-destructive manner.

To improve the sensitivity, the quality of the resonator can still be optimized to achieve higher signal to noise by increasing Q value. Another consideration is the use of attenuators in the mixing chamber to cut out white noise. The amplifier circuit can also be optimized, e.g. the current and voltage noise should be balanced out for maximal performance, which is achieved by adjusting the tap ratio of the capacitors connected at the gate.

References

[1] P. M. Platzman and M. I. Dykman. "Quantum Computing with Electrons Floating on Liquid Helium". In: *Science* 284.5422 (June 18, 1999). Publisher: American Association for the Advancement of Science, pp. 1967–1969. DOI: 10.1126/science.284.5422.1967. URL: https://www.science.org/doi/10.1126/science.284.5422.1967 (visited on 02/08/2023).

[2] Erika Kawakami, Asem Elarabi, and Denis Konstantinov. "Image-Charge Detection of the Rydberg States of Surface Electrons on Liquid Helium". In: *Physical Review Letters* 123.8 (Aug. 19, 2019). Publisher: American Physical Society, p. 086801. DOI: 10.1103/PhysRevLett.123.086801. URL: https://link.aps.org/doi/10.1103/PhysRevLett.123.086801 (visited on 03/08/2023).

[3] Yuriy Monarkha and Kimitoshi Kono. "Two-Dimensional Interface Electron Systems". In: *Two-Dimensional Coulomb Liquids and Solids*. Ed. by Yuriy Monarkha and Kimitoshi Kono. Springer Series in Solid-State Sciences. Berlin, Heidelberg: Springer, 2004, pp. 1–63. ISBN: 978-3-662-10639-6. DOI: 10.1007/978-3-662-10639-6_1. URL: https://doi.org/10.1007/978-3-662-10639-6_1 (visited on 01/06/2023).

[4] Shan Zou. "Detection of the Rydberg States of Electrons on Superfluid Helium Confined in Microchannel Devices". PhD thesis. 2022.

[5] Milton W. Cole and Morrel H. Cohen. "Image-Potential-Induced Surface Bands in Insulators". In: *Physical Review Letters* 23.21 (Nov. 24, 1969). Publisher: American Physical Society, pp. 1238–1241. DOI: 10.1103/PhysRevLett.23.1238. URL: https://link.aps.org/doi/10.1103/PhysRevLett.23.1238 (visited on 03/06/2023).

[6] V. B. Shikin. "Motion of helium ions near a vapor-liquid surface". In: *Sov. Phys. JETP* 31.936 (1970), p. 3.

[7] R. Williams and R. S. Crandall. "Deformation of the surface of liquid helium by electrons". In: *Physics Letters A* 36.1 (Aug. 2, 1971), pp. 35–36. ISSN: 0375-9601. DOI: 10.1016/0375-9601(71)90051-X. URL: https://www.sciencedirect.com/science/article/pii/037596017190051X (visited on 02/26/2023).

[8] W. T. Sommer and David J. Tanner. “Mobility of Electrons on the Surface of Liquid ^{4}He”. In: *Physical Review Letters* 27.20 (Nov. 15, 1971). Publisher: American Physical Society, pp. 1345–1349. DOI: 10.1103/PhysRevLett.27.1345. URL: https://link.aps.org/doi/10.1103/PhysRevLett.27.1345 (visited on 03/06/2023).

[9] R. S. Crandall and R. Williams. “Properties of Electron Surface States on Liquid Helium”. In: *Physical Review A* 5.5 (May 1, 1972). Publisher: American Physical Society, pp. 2183–2190. DOI: 10.1103/PhysRevA.5.2183. URL: https://link.aps.org/doi/10.1103/PhysRevA.5.2183 (visited on 03/06/2023).

[10] Milton W. Cole. “Electronic surface states of liquid helium”. In: *Reviews of Modern Physics* 46.3 (July 1, 1974). Publisher: American Physical Society, pp. 451–464. DOI: 10.1103/RevModPhys.46.451. URL: https://link.aps.org/doi/10.1103/RevModPhys.46.451 (visited on 03/06/2023).

[11] C. C. Grimes and G. Adams. “Evidence for a Liquid-to-Crystal Phase Transition in a Classical, Two-Dimensional Sheet of Electrons”. In: *Physical Review Letters* 42.12 (Mar. 19, 1979). Publisher: American Physical Society, pp. 795–798. DOI: 10.1103/PhysRevLett.42.795. URL: https://link.aps.org/doi/10.1103/PhysRevLett.42.795 (visited on 03/07/2023).

[12] S. A. Lyon. “Spin-based quantum computing using electrons on liquid helium”. In: *Physical Review A* 74.5 (Nov. 30, 2006). Publisher: American Physical Society, p. 052338. DOI: 10.1103/PhysRevA.74.052338. URL: https://link.aps.org/doi/10.1103/PhysRevA.74.052338 (visited on 03/01/2023).

[13] D. I. Schuster et al. “Proposal for Manipulating and Detecting Spin and Orbital States of Trapped Electrons on Helium Using Cavity Quantum Electrodynamics”. In: *Physical Review Letters* 105.4 (July 23, 2010). Publisher: American Physical Society, p. 040503. DOI: 10.1103/PhysRevLett.105.040503. URL: https://link.aps.org/doi/10.1103/PhysRevLett.105.040503 (visited on 03/10/2023).

[14] Brian D’Urso. “Cooling and Self-Excitation of a One-Electron Oscillator”. PhD thesis. Harvard University, 2003.

[15] Jack DiSciaccia. “First Single Particle Measurements of the Proton and Antiproton Magnetic Moments”. PhD thesis. 2013. URL: https://dash.harvard.edu/handle/1/11095961 (visited on 03/11/2023).

[16] Steven R. Jefferts et al. “Superconducting resonator and a cryogenic GaAs field-effect transistor amplifier as a single-ion detection system”. In: *Review of scientific instruments* 64.3 (1993). Publisher: American Institute of Physics, pp. 737–740.

[17] Gerwin Koolstra, Ge Yang, and David I. Schuster. "Coupling a single electron on superfluid helium to a superconducting resonator". In: *Nature Communications* 10.1 (Nov. 22, 2019). Number: 1 Publisher: Nature Publishing Group, p. 5323. ISSN: 2041-1723. DOI: 10.1038/s41467-019-13335-7. URL: https://www.nature.com/articles/s41467-019-13335-7 (visited on 03/08/2023).

[18] H. Zu, W. Dai, and A. T. A. M. de Waele. "Development of dilution refrigerators—A review". In: *Cryogenics* 121 (Jan. 1, 2022), p. 103390. ISSN: 0011-2275. DOI: 10.1016/j.cryogenics.2021.103390. URL: https://www.sciencedirect.com/science/article/pii/S001122752100148X (visited on 02/06/2023).

[19] S. Zou and D. Konstantinov. "Image-charge detection of the Rydberg transition of electrons on superfluid helium confined in a microchannel structure". In: *New Journal of Physics* 24.10 (Oct. 2022). Publisher: IOP Publishing, p. 103026. ISSN: 1367-2630. DOI: 10.1088/1367-2630/ac9696. URL: https://dx.doi.org/10.1088/1367-2630/ac9696 (visited on 03/01/2023).